Investigation of soot formation in n-dodecane spray flames using LES and a discrete sectional method

Available online at www.sciencedirect.com

ScienceDirect

Proceedings of the Combustion Institute 39 (2023) 2587–2597

Proceedings of the Combustion Institute

www.elsevier.com/locate/proci

Investigation of soot formation in *n*-dodecane spray flames using LES and a discrete sectional method

Hesheng Bao*, Abhijit Kalbhor, Noud Maes, Bart Somers, Jeroen Van Oijen

Department of Mechanical Engineering, Eindhoven University of Technology, Eindhoven, 5600 MB, the Netherlands

Received 3 January 2022; accepted 11 July 2022
Available online 28 August 2022

Abstract

Considering stricter regulations on soot emissions, the detailed soot modeling approaches facilitating prediction of soot particle size distributions (PSD) are increasingly in demand. In this context, the transient evolution of soot is numerically investigated for two high-pressure turbulent sprays from the Engine Combustion Network (ECN), namely, Spray C (SC) and Spray D (SD). The $900 - K$ ambient temperature (T_{am}) sprays are studied. This is because the two cases tend to produce a similar amount of soot at $T_{am} = 900K$, despite the significantly different spray development. To predict the soot formation with information on PSD, a discrete sectional method is applied within the large-eddy simulation (LES) framework. The applied modeling strategy favorably captures the experimentally observed similar soot mass for SC and SD in the characteristic field-of-view (FOV) frustum. Moreover, the transient dynamics of soot within the FOV frustum is well captured, and the onset of soot is well predicted. It is observed that for SC and SD, soot formation is more prominent in fuel-rich ($2 < \phi < 4$) and high-temperature ($T > 1500K$) regions. Despite the stronger fuel dilution in the downstream area of the spray, soot is predominantly present in the head of the spray during the whole combustion progress, corresponding to larger particle sizes and higher soot number density. Although the spray development of SC and SD are different, the FOV approach bridges the two cases. The unique correlation between soot mass and FOV volume recognized in experiments was found to hold for the complete quasi-steady sooting region. Moreover, PSD analysis suggests very similar soot size and number density with respect to the FOV volume. This is attributed to the similar LOL for SC and SD in the normalized coordinates, and the same FOV volume corresponding to similar locations in the normalized coordinates.

Keywords: Engine combustion network; Sooting sprays; Discrete sectional method; Large-eddy simulation; Flamelet generated manifolds

1. Introduction

The increasingly harsher legislation regarding soot emissions motivates the demand for accurately

* Corresponding author.
E-mail address: h.bao@tue.nl (H. Bao).

https://doi.org/10.1016/j.proci.2022.07.089

modeling particulate matter with more detail, such as particle size distributions (PSD). To predict soot formation in engines is very challenging owing to the complex in-cylinder physics. In turbulence, soot formation is a combination of soot dynamics which is dependent on combustion and flow characteristics, such as local fuel-air mixing and turbulence time scales [1]. For the igniting sprays studied in the present work, soot formation is closely coupled to spray development and ignition behavior [2,3]. This raises computational challenges and requires high-fidelity models for both the turbulence and combustion. The Engine Combustion Network (ECN) [4] provides extensive characterization of the mixing and combustion processes for sprays at various engine-relevant conditions using different facilities, and comparisons of the corresponding numerical results. Recently, Spray C (SC) and Spray D (SD) were proposed to understand the effects of cavitation on soot emissions.

As expected, soot formation of both SC and SD are sensitive to the ambient temperature. Specifically, at around $900 - K$ ambient temperature (the conditions studied in the current work), the relative amount of soot produced for these injectors changes [5]. The significant difference observed in soot formation weakens, despite the significantly different spray development. This trend was attributed to their similar equivalence ratio distributions at the lift-off length (LOL) [5,6]. From the perspective of numerical investigation, this presents a fascinating and more challenging scenario of spray-flame-soot interactions.

As the current PSD measurements at high-pressure conditions are mostly intrusive and may influence the detected results, only limited experimental information on the PSD is available [7,8]. To enable the information on soot PSD, the detailed soot modeling of turbulent flames mainly relies on the method of moments or discrete sectional method. In the former, each desired property of the PSD is represented by a moment, and usually, several moments are transported. However, the resulting moment model closure remains a mathematical challenge, which has been the subject of several studies [9–11]. The sectional method, on the other hand, facilitates a discrete representation of soot PSD with representative particulate sizes or mass such that the dynamics of soot particles are directly calculated [12]. Numerous investigations in zero-dimensional reactors [13,14], and laminar flames [15,16] proved the high-fidelity of the sectional method. Nevertheless, its accuracy highly correlates with the number of sections adopted. The igniting sprays involve multi-phase flow with various spatio-temporal scales associated with mixing, jet breakup, and evaporation. It is preferable to apply a large-eddy simulation (LES) for its better description of turbulent mixing and finer transient vortical structures when compared to Reynolds-Averaged NavierStokes (RANS) approach. However, efforts on the application of sectional models in turbulent sooting flame within the framework of LES are relatively scarce [17,18] considering the high computational cost of LES in conjunction with the large number of sections required. This is especially the case when complex chemistry is involved. In the context of engine-relevant sprays, the sectional method is mostly applied in a RANS approach [19,20]. The application of LES is so far limited to semi-empirical two-equation-based soot models wherein information about PSD is absent [21]. Moreover, the fidelity of two-equation-based models highly correlates with the parameters applied and must be tuned depending on cases. To the authors' best knowledge, the sectional method is not yet explored within an LES framework to predict soot formation in igniting sprays.

Against these backgrounds, the present study first aims to accurately predict the spray development and ignition process. The transient evolution of soot formation for SC and SD are then predicted with detailed information regarding PSD. The impact of spray characteristics on soot formation is facilitated. These aims are realized by integrating the discrete sectional soot model within an LES framework.

2. Modeling approach

2.1. Spray modeling

The present simulations are performed using OpenFOAM. The Lagrangian-Eulerian approach is adopted for spray modeling. The gaseous phase is described by spatially filtered transport equations of mass, momentum, and the scalars required for combustion modeling. The subgrid scale is closed by the Dynamic Structure LES. Both temporal- and diffusive terms are discretized by implicit second-order schemes, while the convective terms use a Gauss Gamma scheme. The liquid phase is surrounded by the Lagrangian particle tracking approach. The primary breakup is described by a Rosin-Rammler size distribution, and the secondary breakup is modeled by the Kelvin-Helmholtz and Rayleigh-Taylor instabilities. The droplet evaporation and heat transfer with the surroundings are employed by the Frossling model and Ranz-Marshall correlation, respectively. Details of the model implementations are available from previous work [6].

2.2. Combustion modeling

The Flamelet Generated Manifold (FGM) method is adopted in the present study for combustion modeling [22]. In FGM, a manifold rep-

resenting the thermochemical space, parametrized by suitable controlling variables, is constructed from solutions of laminar flamelets. Here, archetypal igniting counterflow diffusion flamelets are computed with detailed chemical kinetics using CHEM1D [23] where a discrete sectional method-based soot model is coupled [16]. A reduced kinetic scheme as described by Wang et al. [24], containing 100 species and 432 reactions, is adopted for the computation of flamelets. In turbulent flames, intermittent soot structures were found to be strongly impacted by scalar dissipation rates χ [25]. Therefore, incorporation of χ in FGM is expected to improve the prediction of soot dynamics. In the igniting flamelet formulation, χ varies in time, and its progress during ignition depends on the applied strain rate a. In this investigation, the evolution of χ is explicitly recorded in the database for several a values and adopted as an additional controlling variable besides the standard mixture fraction Z and reaction progress variable $\mathcal{Y}$. The selected strain rates range from $50s^{-1}$ to the ignition limit corresponding to SC and SD conditions. The thermochemical data of the set of computed unsteady flamelets is tabulated on a uniform mesh with $300 \times 500 \times 8$ grid points in parameter space $Z \times \mathcal{Y} \times a$, respectively. The turbulence-chemistry interaction is realized via a top-hat filtering probability density function applied to the mixture fraction. The closure of filtered source terms (including soot) is accomplished through a transport equation of mixture fraction variance, where the turbulent scalar dissipation is encountered. The details of the FGM modeling approach are available in [6].

2.3. Soot modeling

The soot model employed in the present study is based on the discrete sectional method. In sectional models, soot particle volume ranges are divided into a finite number of n_s sections using an univariate description. Nucleation is modeled based on PAH (A4 here) dimerization. Surface growth and oxidation of soot particles are described through the standard HACA mechanism [26]. PAH condensation is modeled as the coalescence of PAH with soot particles, while coagulation is assumed to occur through the coalescence between soot particles. The specifics of the flamelet sectional soot model can be found in [16]. The retained soot model has been validated for laminar flames in previous works [16,27].

For the computationally efficient LES application of the sectional methods in conjunction with FGM, the reduction in the sectional dimensions is achieved by adopting the clustering (grouping) strategy. Accordingly, 1-D counterflow flamelets for the database creation are computed with complete soot kinetics using $n_s = 60$ by accounting for the mass exchange between the soot and gas phase. In LES, however, transport equations are solved for soot mass fraction in a reduced number, n_c, of clustered sections instead of n_s by assuming the preservation of soot PSD within the clustered section. The filtered equations for soot mass fraction ($Y^c_{s,i}$) in the i-th clustered section read:

$$\frac{\partial \bar{\rho}\widetilde{Y}^c_{s,i}}{\partial t} + \frac{\partial \bar{\rho}\widetilde{u}_j \widetilde{Y}^c_{s,i}}{\partial x_j} - \frac{\partial}{\partial x_j}\left[\bar{\rho} C_{\mathrm{th}} \bar{\nu} \frac{1}{\widetilde{T}} \frac{\partial \widetilde{T}}{\partial x_j} \widetilde{Y}^c_{s,i}\right] = \frac{\partial}{\partial x_j}\left[\bar{\rho}\frac{\nu_{\mathrm{sgs}}}{Sc_{\mathrm{sgs}}} \frac{\partial \widetilde{Y}^c_{s,i}}{\partial x_j}\right] + \rho_s \bar{\dot{Q}}^c_{s,i}, \quad (1)$$

where ρ, ρ_s ν, Sc, and T denote the gas density, constant soot density, kinematic viscosity, Schmidt number, and temperature, respectively. The subscript sgs corresponds to the subgrid scale components. The third term on the left hand side refers the thermophoresis of soot particles (with $C_{\mathrm{th}} = 0.55$), while molecular diffusion of soot is neglected.

The mean source term $\bar{\dot{Q}}^c_{s,i}$ for the corresponding clustered section accounts for combined contributions from nucleation, condensation, surface growth, oxidation, and coagulation sub-processes. The soot source term is tabulated in the lookup database as a production rate and a linearized consumption rate of soot volume fraction and, subsequently, applied in Eq. (1). In this investigation, filtered soot equations are solved for only 6 (90% reduction in sectional dimensions) uniformly clustered sections, and a reconstruction procedure is applied to recover the original distribution of soot mass for all the 60 non-clustered soot sections. This integration of sectional soot method and FGM approach has been verified in the laminar diffusion flames for its accuracy in soot and PSD prediction in comparison with detailed kinetics counterparts [28], and is extended for turbulent combustion applications in the present study. This soot modeling strategy facilitates a drastic reduction in the number of transport equations (hence CPU cost) with a low memory footprint of the FGM database. For instance, in the current simulations, doubled number of the clustered sections corresponds to approximately a 25% increment in computational time with an additional 30% increase in the database size.

3. Case description and numerical setup

To validate the turbulence predictions of SC and SD, the non-reacting (0% O_2) ECN Spray A (SA) case is simulated as a comparison. SC and SD are simulated for both non-reacting and reacting (15% O_2) conditions. All cases have the same ambient temperature ($900K$) and density ($22.8kg/m^3$), and the same fuel temperature ($363K$) at $150MPa$ injection pressure. The nozzle diameter D_{noz} and discharge coefficient C_d, however, are different among the cases, see Table 1. Note that the spreading angles for SA, SC, and SD are set as 21, 21.5, and

Table 1
Case specifications.

Case number	O_2 [% vol.]	D_{noz} [μ m]	C_d [-]	d_{eq} [μ m]	t_{inj} [μ s]
1 (SA)	0	90	0.89	489	-
2 (SC)	0	200	0.81	1032	-
3 (SD)	0	186	0.97	1066	-
4 (SC)	15	200	0.81	1032	5
5 (SD)	15	186	0.97	1066	5

19 degrees, following literature [29,30]. A uniform structured mesh with hexahedral elements is applied for all three cases and validated in previous work [6]. Since soot evolution takes significantly longer than ignition, the mesh length adopted in the present study is increased to 150*mm* to allow for extended flame development. The mesh expansion ratio is reduced to 1.005 along the spray direction, resulting in a more refined mesh in the upstream region when compared to the previous mesh used in [6].

4. Model validation

4.1. Non-reacting spray

The spray modeling approach that was previously shown to well capture the liquid penetration (LP) and vapor penetration (VP) [6], is first applied for non-reacting sprays, *i.e.*, Case 1, 2, and 3 listed in Table 1. The results are quantitatively validated via the experiments. In the present study, the prediction of the local mixture fraction Z_x, is evaluated. Although spatial Z distributions for SC and SD are not yet available from experiments, the established SA measurements allow for an investigation. It was shown that the vapor fuel distribution for the three configurations studied in the present work collapse when so-called comparable entrainment coordinates are used [31]. The spatial coordinates are thus normalized by the equivalent nozzle diameter $d_{eq} = d_e\sqrt{\rho_f/\rho_a}$ for comparison. Here, d_e is the effective nozzle diameter which takes cavitation into account [31]. ρ_f and ρ_a are fuel and ambient densities, respectively. Fig. 1 shows the predicted radial Z distribution (averaged from 1.5 to 3 ms) in normalized coordinates with the SA measurements at three characteristic distances from the injection tip, from spatially upstream of the SA lift-off length LOL (the shortest LOL among the three cases) until approximately two times the SD LOL (the longest LOL). The value at each radial location is an azimuthal average of 90 slices of time-averaged fields along the spray axis. The results suggest good agreement to the experiment for both SC and SD. Both the global transient spray development and local time-averaged Z distribution are well captured. This gives confidence to the soot predictions, as soot formation is strongly determined by local mixing.

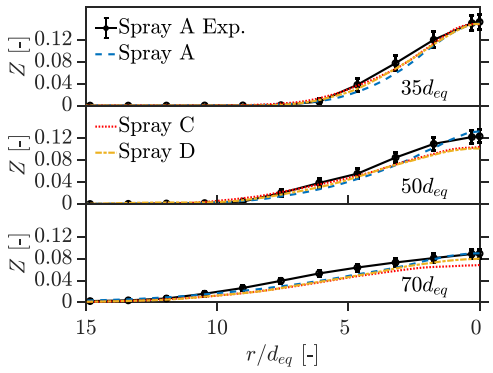

Fig. 1. Time-averaged mixture fraction distribution of non-reacting sprays at three characteristic distances from the injection tip, with the coordinates normalized by the corresponding equivalent nozzle diameter.

4.2. Reacting spray

Being an important combustion indicator, the predicted ignition behavior for SC and SD (Case 4 and 5 in Table 1) are evaluated. The predicted ignition delay time (IDT) for SC and SD are 0.538 and 0.544ms, respectively, and compare reasonably well to the experimental values, 0.561 and 0.563 ms [5]. The predicted lift-off lengths (LOL) for SC and SD are 23.1 and 26.0mm, respectively. The simulation reproduces the experimentally observed trends of both the similar IDT and the different LOL between SC and SD. Both numerical values are defined following [6]. The transient flame structure evolution is depicted in Fig. 2 by sampling the simulated data on a plane crossing the spray axis within the flame envelope at several representative time instances. The most upstream region in which low-temperature combustion is found, indicated by the contour of 0.001 times the maximum $C_12H_25O_2$ mass fraction during simulation (in black), for both cases is found to stabilize very quickly. The spray tip of $C_12H_25O_2$, on the other hand, travels downstream until high-temperature combustion occurs, coinciding with the consumption of the low-temperature combustion products. This is consistent with literature [32]. For both cases, the high-temperature ignition kernels ($T > 1500K$) initialize at the periphery of the flame and propagate simultaneously both upstream to the quasi-steady LOL location and downstream until it reaches the spray tip.

5. Results and discussion

In this section, the results of the clustered sectional soot model are discussed given the fact that

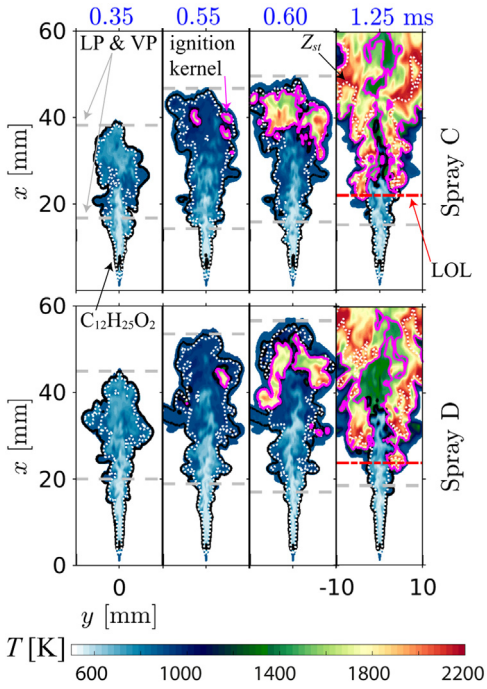

Fig. 2. Temporal evolution of temperature within the flame envelope for representative time instances with additional contours identifying: stoichiometry (white dotted line), 0.1% of the maximum mass fraction threshold for $C_12H_25O_2$ (black contour), $T = 1500K$ (magenta contour), LP and VP (grey dashed line), and LOL (red dash-dotted line). (For interpretation of the references to colour in this figure legend, the reader is referred to the web version of this article.)

both mixing and ignition behavior, being the primary challenges in modeling igniting soot-laden flames, are well predicted by the currently used model. The results are first compared to the available experimental data on soot mass, followed by further discussions on local characteristics.

5.1. Soot mass results

The experimental soot mass in this section includes the results obtained by facilities at three different institutions, including a constant-pressure vessel at the Spray Combustion Laboratory at Caterpillar (Caterpillar), and two constant-volume pre-combustion chambers at Sandia National Laboratories (Sandia) and IFP Energies Nouvelles (IFPEN), respectively. To create an unambiguous comparison of the soot mass between SC and SD in different experimental setups (with different window dimensions) at a range of different ambient temperatures, a fixed field-of-view (FOV) approach is introduced in ECN experiments [4,5]. With this approach, the soot mass is determined in a certain volume using a conical frustum starting from the corresponding soot inception point.

Fig. 3(a) compares the simulated evolution of soot mass for SC and SD in a 6000-mm^3 FOV frustum starting at the soot inception location with corresponding results measured in three different facilities. The results of simulations and experiments by three institutions are marked by four different colors, which also applies in 3(b) and (c). Note that a higher soot mass in the Caterpillar experiments is at least partially explained by the experimental ambient gas composition without CO_2 and H_2O in that case [5]. In the simulations, the ambient gas composition of the Sandia experiments is reproduced. The trend of soot mass development in the FOV field is reasonably captured, including the initialization indicated by τ_1, followed by a peak notated by τ_2, and the start of a quasi-steady soot mass phase marked by τ_3. In addition to the effects caused by CO_2 and H_2O in the ambient gas, the model constants used in [27] for the well-established ethylene flame are used without adoption. For the current spray flame, the surface growth rate may be different. Additionally, the enhanced soot aggregation due to a higher pressure [33], and larger particles [8] are not included. Nevertheless, capturing the general trend of soot behavior with fair agreement of the total soot mass compared to the experiments (considering significant differences in absolute values between experiments too) promotes the application of the current modeling approach. The transient soot inception location for SC and SD are shown in Fig. 3(c) and again agree well with the experiments. The representative colors adopt the legend from Fig. 3(a). The end of the 6000 $-$ mm^3 FOV frustum for the simulation is also marked. At the same time, these panels show the radially integrated intensity of soot mass (Ism) along the spray axis (x) in a so-called Ism_{xt}-plot (similar to the I_{xt}-plot discussed by Maes et al. [34]). The soot mass production is observed to be confined by the vapor penetration that is marked by yellow cross markers, which agree well to the measurements indicated by the yellow dashed line with standard deviations. It is noted that the inception of soot is defined as the location where 0.01 $-$ μg Ism_x is observed following the experiments.

Fig. 3(b) shows the relationship of the averaged quasi-steady soot mass between 2.5 and 5ms, and the chosen FOV volume. Note, again, how a factor of two difference between the soot mass here may be explained by the different ambient gas composition, and model assumptions discussed above. The unique correlation between soot mass and FOV volume within the optical area in experiments was pointed out in [5], potentially allowing for the evaluation of the soot mass in an extend FOV through extrapolation. Indeed, the leveling-off seen in Caterpillar experimental data is due to the end of the FOV at approximately 77mm downstream of the injector tip. Here, the simulated

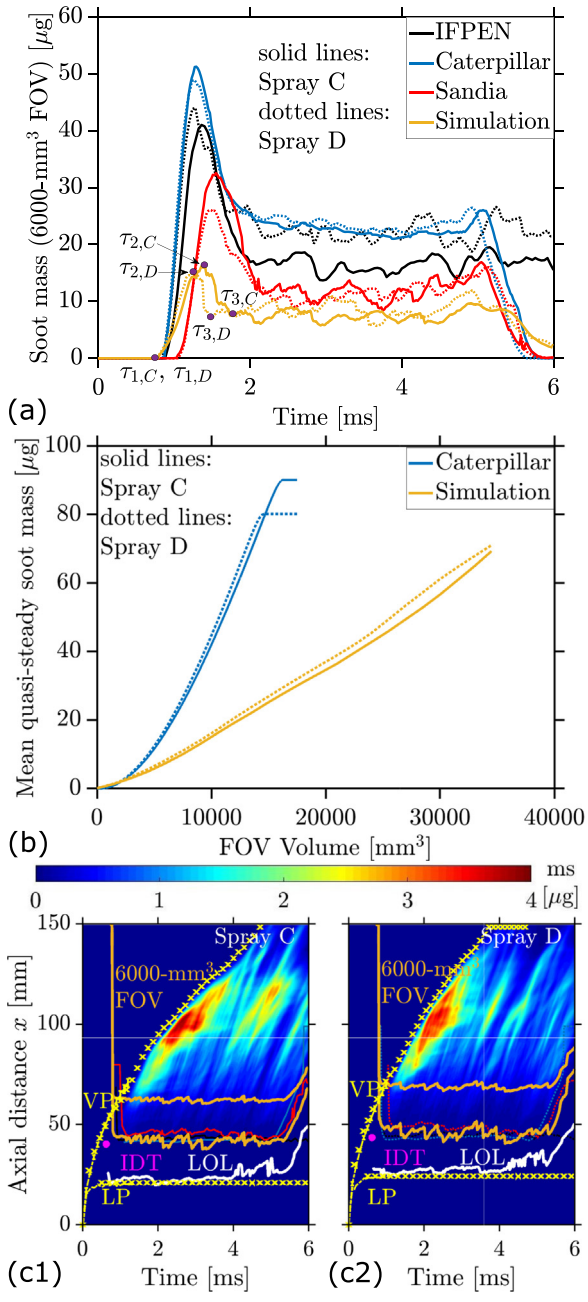

Fig. 3. Comparison of global soot behavior between simulation and experiments: (a) evolution of soot mass in a 6000-mm^3 frustum, (b) relationship between time-averaged soot mass and FOV volume, (c) Ism_{xt}-plot of simulated soot mass with soot inception and the end of the 6000-mm^3 FOV volume identified by orange lines (1. Spray C, 2. Spray D). Experimental soot inception locations are identified by their representative colors from the legend of figure (a). The dashed lines with standard deviations mark the experimental VP and LP, while the corresponding simulated values are shown by cross markers. The experimental data is taken from [5].

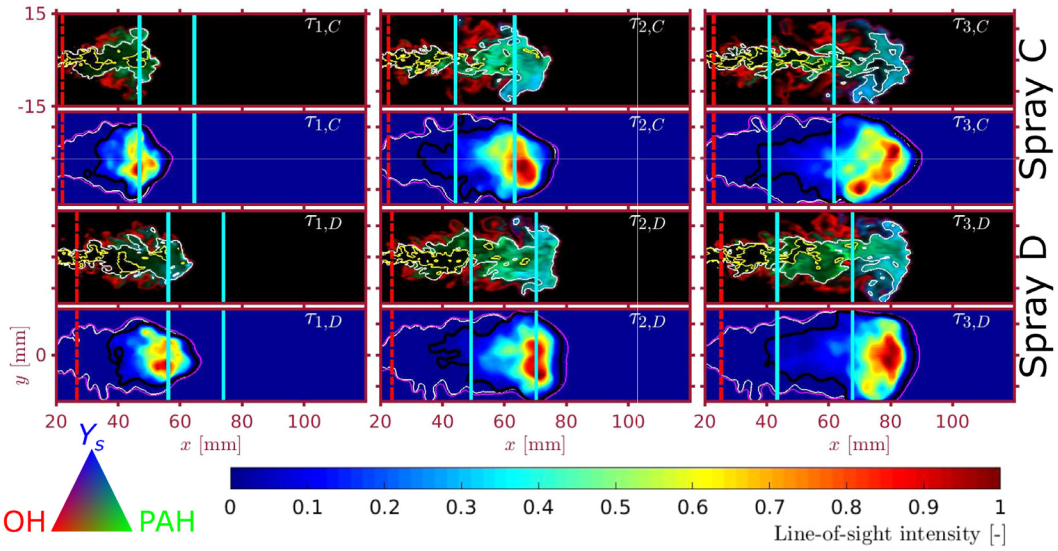

Fig. 4. Temporal evolution of simulated soot mass distributions at selected time instances. First (SC) and third (SD) rows: color plots of OH (red), PAH (green), and soot mass fraction (Y_s, blue) on a cross-section along the spray axis. All presented species are normalized by their maximum values found on the selected plane. Second and fourth rows: false-color images of line-of-sight integrated soot mass with a 6000-mm^3 FOV field indicated by the cyan lines and projected spray envelope marked by the magenta line. Note that the white lines, $\phi = 2$ contours, refer to the ϕ value on the plane (first and third row), and the line-of-sight density-averaged ϕ within the flame volume in the line-of-sight integrated panels (second and fourth row), respectively. The yellow lines refer to $\phi = 4$ contours. The black lines mark 0.1% of the maximum line-of-sight soot mass per panel. (For interpretation of the references to colour in this figure legend, the reader is referred to the web version of this article.)

result up to approximately 100mm is shown, where a correlation still exists. An even larger FOV volume may not make sense, given that the spray tip only develops to about 110mm for SD at 2.5ms, and that the soot mass, as observed in the upper-right corner of the Ism_{xt}-plot, is oxidized in these downstream areas. The low intensity seen in the upper-right corner also indicates that the 150mm length adopted in the present study is sufficiently long to capture the soot development. It was previously pointed out by Maes et al. [5] that SC generally produces more soot than SD at higher ambient temperatures, while SC tends to be slightly less sooting at temperatures of approximately 900K and below. Fig. 3(b) shows a slightly higher soot amount for SD at 900K, which coincides with the experimental observation. Also, the VP and LP penetrations, defined as the farthest axial distance from the nozzle outlet with the gaseous fuel mass fraction of 0.001 and that where the projected liquid volume of 0.2×10^{-3} mm^3 liquid/mm^2 is found, respectively, are shown in the Ism_{xt}-plots. The results illustrate very good agreement between the predictions and the experiments.

5.2. Soot formation

The local soot characteristics within the spray envelope are analyzed in detail in this section. The soot formation at three representative time instances as indicated by τ_1 through τ_3 in Fig. 3 are shown in Fig. 4 from left to right. For visibility, the key species mass fraction distribution including soot (Y_s), OH, and PAH on a cross-section on the spray axis are colored by blue, red, and green, respectively. The combinations of three species lead to new colors that are indicated in the legend in the lower-left corner. The line-of-sight soot values at a certain time are normalized by the maximum of their values in the panel. This is because the magnitude of local soot mass continuously increases as the flame develops. Especially at τ_1, the soot inception timing, the magnitude of local soot mass is extremely low compared to the later stage.

The color plots of species illustrate that soot formation is closely related and partially overlapping with PAH. As expected, PAH hardly coincides with OH, as coalescing PAH are required to initialize nascent soot formation while OH oxidizes the soot and PAH. The prevalence of OH in relatively leaner mixtures (around equivalence ratio $\phi = 1$) forces the soot to remain in richer mixtures. A quantitative analysis implies that soot is mostly bound within the area rendered by $2 < \phi < 4$, which is consistent with observations in literature [35]. It is observed that for both τ_2 and τ_3, the 6000-mm^3 FOV volume (indicated by the cyan

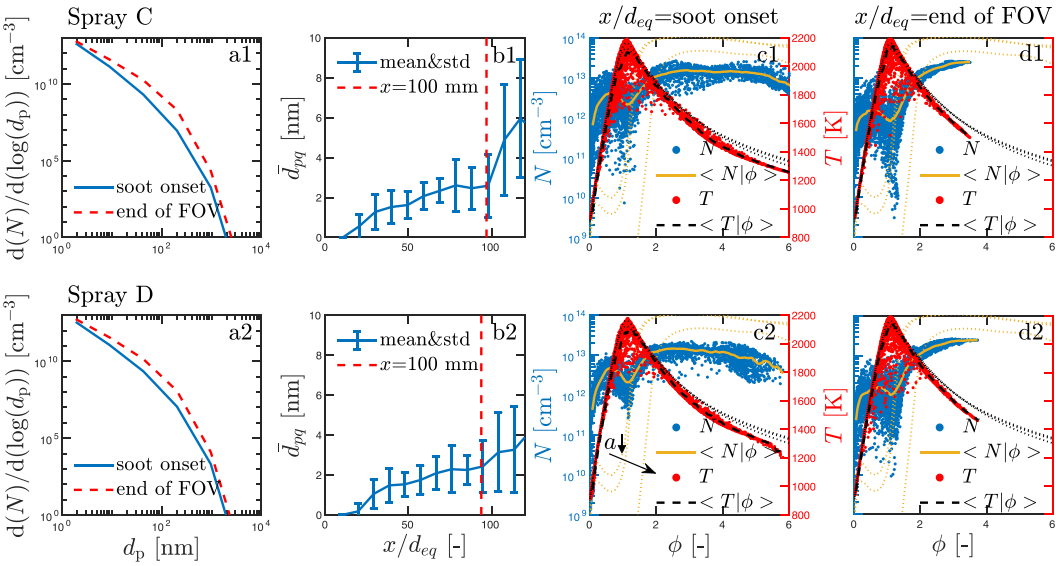

Fig. 5. Particle size distributions for SC (top) and SD (bottom): (a) time-averaged PSD at the spray axis, (b) ensemble-averaged diameters of the particles along the spray axis, (c) and (d) distributions of soot number density N and T in ϕ-space with their conditional average with respect to ϕ at 2.5 ms for two different axial distances from the injection tip. As comparisons, results of characteristic steady flamelets are shown in (c) and (d) by dotted lines.

lines) does not capture the most intensive soot region.

By introducing the density-averaged equivalence ratio in the second and fourth row (indicated by the black contours using a criterion of 0.1% of the maximum line-of-sight soot mass per panel), it is confirmed that the soot formation is confined within the $\phi > 2$ region. The soot mass is the highest in the head of the spray for all time instances, ultimately limited by the high-temperature flame. A quantitative analysis on line-of-sight soot mass suggests that at τ_2, the soot mass in the 6000-mm^3 FOV volume for SC and SD are 16.2 and 15.3 μ g, respectively, corresponding to 53.2% and 61.0% of the instantaneous total soot mass in the domain. For brevity, this percentage is represented by α_{FOV}. At τ_3, α_{FOV} for SC and SD reduce to 12.3 and 15.98%, respectively. In general, for both cases, the value of α_{FOV} starts to decrease when the soot head develops to the downstream of the FOV field. Finally, α_{FOV} stabilizes at a value that is lower than 10, i.e. more than 90% of soot mass is located out of the 6000-mm^3 FOV volume, for both cases when the quasi-steady soot formation is reached. The period between the initialization and stabilization of α_{FOV} change are 1.2 and 0.85ms for SC and SD, respectively. This can be attributed to the faster axial spray development of SD. However, the soot inception for SC and SD spatially follow the LOL (an increased LOL of SD corresponds to a farther downstream soot inception location), while their initialization times are similar (similar IDT).

5.3. Particle size distributions

The calculated soot PSD for SC and SD are analyzed and shown in Fig. 5. The PSD is first evaluated at the location of the start and end of the 6000-mm^3 FOV volume for SC and SD, respectively in Fig. 5(a1) and Fig. 5(b1). A time-averaged PSD between 2.5 and 5 ms is adopted. It is seen that the two cases have similar PSD at the same location with respect to the FOV volume. This can be attributed to the similar LOL/d_{eq} for SC and SD, meaning that they have similar equivalence ratio distributions at the LOL and thus similar soot behavior. The same FOV volume for the two cases lead to a similar x/d_{eq}. Fig. 5(b) presents the ensemble-averaged diameters of the particles $\bar{d}_{63} = (\sum_{j=0}^{\infty} N_j d_{\mathrm{p},j}^6 / \sum_{j=0}^{\infty} N_j d_{\mathrm{p},j}^3)^{1/3}$ [36] at the spray centerline between 2.5 and 5ms. It is observed that the two cases have similar particulate size if comparable entrainment coordinates are applied. Larger particles exist in the farther downstream region, corresponding to the higher soot mass observed in Fig. 4. Here, $\bar{d}_{63}$ is adopted following [36] rather than the physical mean diameter. This leads to a relatively smaller particulate diameter compared to the measurements [8]. Fig. 5(c) and Fig. 5(d) show scatter plots of soot number density N and T with their conditional means $\langle N|\phi\rangle$ at the planes corresponding to the soot onset, and end of the 6000-mm^3 FOV at 2.5ms, respectively. In Fig. 6, $\langle N|\phi\rangle$ distribution in ϕ-space at the two respective locations are shown for τ_1, τ_2, τ_3. Also, the flamelet

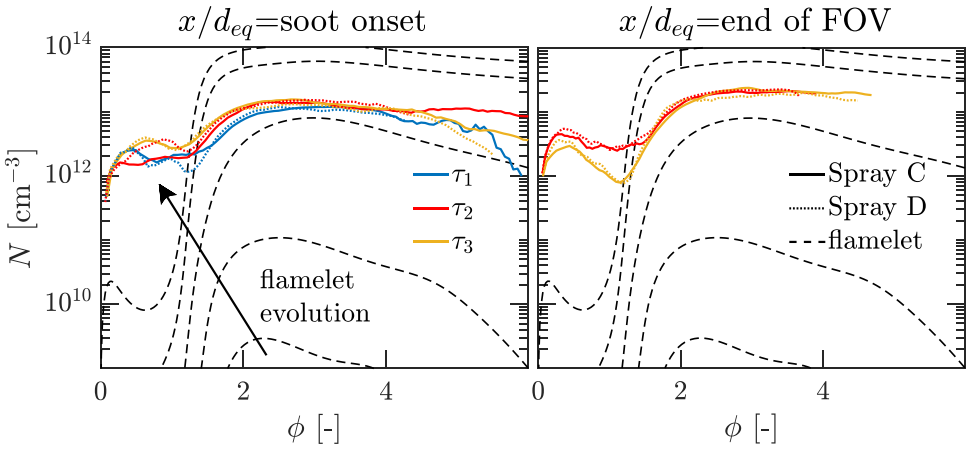

Fig. 6. Soot number density N of SC and SD at τ_1, τ_2, τ_3 and that of the igniting flamelet results at a representative a.

results are shown for comparison. Note that at τ_1 for both SC and SD the sprays have not yet reached the end of the $6000 - mm^3$ FOV. Thus, soot does not exist in Fig. 6(b) at τ_1. For both locations, lower values of N are observed at stoichiometric conditions ($\phi = 1$). The lowest value of $\langle N|\phi\rangle$ decreases as spray develops in time, and at all times spatially decreases towards the downstream spray. $\langle N|\phi\rangle$ shows a more pronounced soot presence in the rich mixtures, which is seen in both the turbulent and flamelet simulations. The soot distribution in ϕ-space is narrower in the downstream area of the sprays. Also, soot occurs in richer mixtures in laminar flames compared to the turbulent sprays. As the spray develops, larger ϕ values do not exist because of the mixing. The difference of N between sprays and flamelets in magnitude mainly exists in lean mixtures whereas the temperatures are comparable. This may be attributed to the difference in time scales. The slowly evolving soot depends significantly on the local turbulence.

6. Conclusions

The present study applied the discrete sectional method in an LES approach for modeling the soot formation in ECN Spray C and Spray D flames. Based on the excellent predictions for non-reacting spray behavior, the combustion indicators were well captured. The sectional modeling of soot was then performed via an ad hoc clustered sectional approach. Promising agreement to experiments was given for soot mass in the FOV volume by directly applying the model constants calibrated for an ethylene flame. The mean soot mass for the quasi-steady stage in the FOV frustum was found to linearly correlate with its volume for both SC and SD, over a much larger axial distance than measured by experiments. Analysis on local soot formation revealed that soot mainly exists when $2 < \phi < 4$ and $T > 1500K$. The soot formation is the most intensive in the spray head during the whole combustion process. Therefore, a decrement in the percentage of soot mass captured by the FOV volume is observed. The soot inception location and time, on the other hand, are related to the LOL and IDT, respectively. PSD analysis suggests very similar soot size and number density for the two cases with respect to the normalized coordinates. In general, the soot particles for both cases are larger in size in the downstream region, while larger soot numbers are found in the rich mixtures.

Declaration of Competing Interest

The authors declare that they have no known competing financial interests or personal relationships that could have appeared to influence the work reported in this paper.

Acknowledgments

The authors gratefully acknowledge the Eindhoven University of Technology for the computational resources.

References

[1] P.G. Arias, V.R. Lecoustre, S. Roy, Z. Luo, D.C. Haworth, T. Lu, A. Trouvé, H.G. Im, Dynamics of flow–soot interaction in wrinkled non-premixed ethylene–air flames, Combust. Theor. Model. 19 (5) (2015) 568–586.

[2] L.M. Pickett, J. Manin, C.L. Genzale, D.L. Siebers, M.P.B. Musculus, C.A. Idicheria, Relationship between diesel fuel spray vapor penetration/dispersion and local fuel mixture fraction, SAE Int. J. Engines 4 (1) (2011) 764–799.

[3] E. Cenker, G. Bruneaux, L. Pickett, C. Schulz, Study of soot formation and oxidation in the engine combustion network (ECN), Spray A: Effects of ambient temperature and oxygen concentration, SAE Int. J. Engines 6 (1) (2013) 352–365.
[4] ECN, Engine Combustion Network, 2021, (https://ecn.sandia.gov/).
[5] N. Maes, S.A. Skeen, M. Bardi, R.P. Fitzgerald, L.-M. Malbec, G. Bruneaux, L.M. Pickett, K. Yasutomi, G. Martin, Spray penetration, combustion, and soot formation characteristics of the ECN Spray C and Spray D injectors in multiple combustion facilities, Appl. Therm. Eng. 172 (2020) 115136.
[6] H. Bao, N. Maes, H.Y. Akargun, B. Somers, Large Eddy Simulation of cavitation effects on reacting spray flames using FGM and a new dispersion model with multiple realizations, Combust. Flame 236 (2022) 111764.
[7] A.E. Karataş, O.L. Gülder, Soot formation in high pressure laminar diffusion flames, Prog. Energ. Combust. 38 (6) (2012) 818–845.
[8] S.A. Skeen, K. Yasutomi, E. Cenker, B. Adamson, N. Hansen, L.M. Pickett, Standardized optical constants for soot quantification in high-pressure sprays, SAE Int. J. Engines 11 (6) (2018) 805–816.
[9] F. Mng.haci, Method of moments with interpolative closure, Chem. Eng. Sci. 57 (12) (2002) 2229–2239.
[10] D.L. Marchisio, R.O. Fox, Solution of population balance equations using the direct quadrature method of moments, J. Aerosol Sci. 36 (1) (2005) 43–73.
[11] M.E. Mueller, G. Blanquart, H. Pitsch, Hybrid method of moments for modeling soot formation and growth, Combust. Flame 156 (6) (2009) 1143–1155.
[12] F. Gelbard, Y. Tambour, J.H. Seinfeld, Sectional representations for simulating aerosol dynamics, J. Colloid Interface Sci. 76 (2) (1980) 541–556.
[13] J.Z. Wen, M.J. Thomson, S.H. Park, S.N. Rogak, M.F. Lightstone, Study of soot growth in a plug flow reactor using a moving sectional model, Proc. Combust. Inst. 30 (1) (2005) 1477–1484.
[14] J.S. Bhatt, R.P. Lindstedt, Analysis of the impact of agglomeration and surface chemistry models on soot formation and oxidation, Proc. Combust. Inst. 32 (1) (2009) 713–720.
[15] M.S. Celnik, M. Sander, A. Raj, R.H. West, M. Kraft, Modelling soot formation in a premixed flame using an aromatic-site soot model and an improved oxidation rate, Proc. Combust. Inst. 32 (1) (2009) 639–646.
[16] C.A. Hoerlle, F.M. Pereira, Effects of CO_2 addition on soot formation of ethylene non-premixed flames under oxygen enriched atmospheres, Combust. Flame 203 (2019) 407–423.
[17] P. Rodrigues, B. Franzelli, R. Vicquelin, O. Gicquel, N. Darabiha, Coupling an LES approach and a soot sectional model for the study of sooting turbulent nonpremixed flames, Combust. Flame 190 (2018) 477–499.
[18] L. Tian, M.A. Schiener, R.P. Lindstedt, Fully coupled sectional modelling of soot particle dynamics in a turbulent diffusion flame, Proc. Combust. Inst. 38 (1) (2021) 1365–1373.
[19] D. Aubagnac-Karkar, J.-B. Michel, O. Colin, P.E. Vervisch-Kljakic, N. Darabiha, Sectional soot model coupled to tabulated chemistry for Diesel RANS simulations, Combust. Flame 162 (8) (2015) 3081–3099.
[20] S. Fontanesi, M. Del Pecchia, V. Pessina, S. Sparacino, S. Di Iorio, Quantitative investigation on the impact of injection timing on soot formation in a GDI engine with a customized sectional method, Int. J. Engine Res. (2021). 1468087421993955
[21] S. Xu, S. Zhong, K.M. Pang, S. Yu, M. Jangi, X.-s. Bai, Effects of ambient methanol on pollutants formation in dual-fuel spray combustion at varying ambient temperatures: A large-eddy simulation, Appl. Energ. 279 (2020) 115774.
[22] J.A. Van Oijen, L. De Goey, Modelling of premixed laminar flames using flamelet-generated manifolds, Combust. Sci. Technol. 161 (1) (2000) 113–137.
[23] B. Somers, The simulation of flat flames with detailed and reduced chemical models, Technische Universiteit Eindhoven, 1994 Ph.D. thesis.
[24] H. Wang, Y. Ra, M. Jia, R.D. Reitz, Development of a reduced n-dodecane-pah mechanism and its application for n-dodecane soot predictions, Fuel 136 (2014) 25–36.
[25] F. Bisetti, G. Blanquart, M.E. Mueller, H. Pitsch, On the formation and early evolution of soot in turbulent nonpremixed flames, Combust. Flame 159 (1) (2012) 317–335.
[26] J. Appel, H. Bockhorn, M. Frenklach, Kinetic modeling of soot formation with detailed chemistry and physics: laminar premixed flames of C2 hydrocarbons, Combust. Flame 121 (1–2) (2000) 122–136.
[27] A. Kalbhor, J. van Oijen, Effects of hydrogen enrichment and water vapour dilution on soot formation in laminar ethylene counterflow flames, Int. J. Hydrogen Energ. 45 (43) (2020) 23653–23673.
[28] A. Kalbhor, D. Mira, J. van Oijen, A computationally efficient approach for soot modeling with discrete sectional method and FGM chemistry, Submitted (2022).
[29] J.V. Pastor, R. Payri, J.M. Garcia-Oliver, J.-G. Nerva, Schlieren measurements of the ecn-spray a penetration under inert and reacting conditions, SAE Tech. Pap. (2012) 2012–01–0456.
[30] F.R. Westlye, M. Battistoni, S.A. Skeen, J. Manin, L.M. Pickett, A. Ivarsson, Penetration and combustion characterization of cavitating and non-cavitating fuel injectors under diesel engine conditions, SAE Tech. Pap. (2016) 2016–01–0860.
[31] J.V. Pastor, J.M. Garcia-Oliver, A. Garcia, A.M. López, An experimental investigation on spray mixing and combustion characteristics for spray C/D nozzles in a constant pressure vessel, SAE Tech. Pap. (2018) 2018–01–1783.
[32] H.S. Sim, N. Maes, L. Weiss, L.M. Pickett, S.A. Skeen, Detailed measurements of transient two-stage ignition and combustion processes in high-pressure spray flames using simultaneous high-speed formaldehyde PLIF and schlieren imaging, Proc. Combust. Inst. 38 (4) (2021) 5713–5721.
[33] B. Gigone, A.E. Karataş, O.L. Gülder, Soot aggregate morphology in coflow laminar ethylene diffusion flames at elevated pressures, Proc. Combust. Inst. 37 (1) (2019) 841–848.
[34] N. Maes, M. Meijer, N. Dam, B. Somers, H.B. Toda, G. Bruneaux, S.A. Skeen, L.M. Pickett, J. Manin, Characterization of Spray A flame structure for parametric variations in ECN constant-volume ves-

sels using chemiluminescence and laser-induced fluorescence, Combust. Flame 174 (2016) 138–151.
[35] M. Pucilowski, M. Jangi, H. Fatehi, K.M. Pang, X.-S. Bai, LES study of diesel flame/wall interaction and mixing mechanisms at different wall distances, Proc. Combust. Inst. 38 (4) (2021) 5597–5604.
[36] Y. Wang, A. Raj, S.H. Chung, Soot modeling of counterflow diffusion flames of ethylene-based binary mixture fuels, Combust. Flame 162 (3) (2015) 586–596.